



1 **Improved representation of river runoff in Estimating the**
2 **Circulation and Climate of the Ocean Version 4 (ECCOV4)**
3 **simulations: implementation, evaluation and impacts to**
4 **coastal plume regions**
5

6 Yang Feng^{1,2,3,7}, Dimitris Menemenlis⁴, Huijie Xue^{1,2}, Hong Zhang⁴, Dustin Carroll^{5,4},
7 Yan Du^{1,2}, Hui Wu⁶
8

- 9 1. State Key Laboratory of Tropical Oceanography, South China Sea Institute of Oceanology, Chinese
10 Academy of Science, Guangzhou, China
11 2. Southern Marine Science and Engineering Guangdong Laboratory, Guangzhou, China
12 3. Institution of South China Sea Ecology and Environmental Engineering, Chinese Academy of
13 Sciences, Guangzhou, China
14 4. Jet Propulsion Laboratory, California Institute of Technology, Pasadena, California, USA
15 5. Moss Landing Marine Laboratories, San José State University, Moss Landing, California, USA
16 6. State Key Laboratory of Estuarine and Coastal Research, East China Normal University, Shanghai,
17 China
18 7. Guangdong Key Laboratory of Ocean Remote Sensing, South China Sea Institute of Oceanology,
19 Chinese Academy of Sciences

20 *Correspondence to:* Yang Feng (yfeng1982@126.com)
21
22



23 **Abstract**

24 In this study, we improve the representation of global river runoff in the Estimating the
25 Circulation and Climate of the Ocean Version 4 (ECCOV4) framework, allowing for a more realistic
26 treatment of coastal plume dynamics. We use a suite of experiments to explore the sensitivity of coastal
27 plume regions to runoff forcing, model grid resolution, and grid type. The results show that simulated
28 Sea-Surface Salinity (SSS) is reduced as the model grid resolution increases. Compared to Soil
29 Moisture Active Passive (SMAP) observations, simulated SSS is closest to SMAP when using Daily,
30 Point-source Runoff (DPR) and the intermediate resolution LLC270 grid. The Wilmott skill score,
31 which quantifies agreement between models and observations, yields up to 0.92 for large rivers such as
32 the Amazon. There was no major difference in SSS for tropical and temperate coastal rivers when the
33 model grid type was changed from ECCO v4 latitude-longitude-polar cap grid to ECCO2 cube-sphere
34 grid. We also found that using DPR forcing and increasing model resolution from the coarse resolution
35 LLC90 grid to the intermediate resolution LLC270 grid elevates the river plume area, volume, and
36 freshwater transport, along with stabilizing stratification and generally shoaling the mixed layer depth
37 (MLD). Additionally, we find that the impacts of increasing model resolution from intermediate
38 resolution LLC270 grid to high resolution LLC540 grid are regionally dependent. The Mississippi
39 River Plume is more sensitive than others regions, possibly because the wider and shallower Texas-
40 Louisiana shelf drives a stronger baroclinic effect, as well as relatively weak sub-grid vertical mixing
41 and adjustment in this region. The results indicate that due to the complex bathymetry and dynamic
42 behaviour of coastal environments, it may be challenging for spatially-unified resolution models to
43 capture process-rich fidelity and obtain computational efficiency for coastal interfaces on a global
44 scale. Our results offer a benchmark for representing Land-Ocean-Aquatic-Continuum (LOAC)
45 processes in global models and data assimilation products and will help advance predictions of land-
46 ocean-atmospheric feedbacks seamlessly in the next generation of earth system models.

47
48
49



50 **1 Introduction**

51 Coastal plume regions represent a small fraction of Earth's surface, and played as an active
52 component in global cycling of carbon and nutrients (Bourgeois et al., 2016; Carroll et al., 2020; Fennel
53 et al., 2019; Lacroix et al., 2020; Landschützer et al., 2020; Roobaert et al., 2019). Recent satellite-based
54 observations with quasi-global coverage has been greatly improved to monitor Sea Surface Salinity, a
55 key tracer for tracking the river plumes. The European Space Agency (ESA) Soil Measure and Ocean
56 Salinity (SMOS, Mecklenburg et al., 2012) with 33 km/10 day and National Aeronautics and Space
57 Administration (NASA) Soil Moisture Active Passive (SMAP) missions with 40 km/8 day space/time
58 gridding are acquiring SSS observations with sufficient resolution to track the plume pathways and
59 evaluate coastal plume dynamics (Fournier et al. 2016a, b; 2017a,b; 2019; Gierach et al. 2013; Liao et
60 al., 2020). To date, however, the coastal plume regions has not been explicitly resolved in most global
61 Ocean General Circulation Models (OGCMs), Earth System Models (ESMs), and Global Ocean Data
62 Assimilation System (GODAS) products (Ward et al., 2020). As a result, the plume region produced by
63 OGCMs, ESMs, and GODAS are not consistent with satellite observations. For example, Fournier et al.
64 (2016a) found that the 1/12° global circulation Hybrid Coordinate Ocean Model (HYCOM) did not
65 accurately capture SSS during extreme flood events in the northern Gulf of Mexico. Denamiel et al.
66 (2013) found that the Congo River nearshore SSS in global HYCOM was underestimated compared to
67 other regional simulations, even though the models had comparable horizontal grid resolution. Santini
68 and Caporaso (2018) suggested that most CMIP5 models might lack skill in representing the Congo River
69 Basin runoff and SSS in the vicinity of river mouths. Most OGCMs, ESMs, and GODAS products usually
70 had large grid cells; a few cells may encompass the entire plume. As a result, water delivered to the cells
71 are fully mixed and diluted, therefore, cannot accommodate the complex dynamics. Additionally,
72 riverine freshwater input to the ocean is forced in the top model layer over a pre-determined surface area
73 in the vicinity of river mouths with climatological signal, thus the system disturbance by extreme weather
74 events, e.g. floods and droughts, cannot be explicitly resolved (Griffies et al. 2005; Tseng et al. 2016).
75 Finally, virtual salt fluxes have been widely employed, where freshwater affects salinity without a change
76 in mass or volume flux (Bentsen, 2013; Halliwell, 2004; Timmermann et al., 2009; Volodin et al., 2010).
77 The above model configurations may limit the representation of coastal plume region in global scale
78 models.



79 Estimating the Circulation and Climate of the Ocean (ECCO) is a data assimilating model that uses
80 observational data to make the best possible estimates of ocean circulation and its role in climate. The
81 model takes the cube-sphere (ECCO2) to latitude-longitude-polar-cap (ECCOv4) grid for global
82 application. Like most OGCMs, ESMs, and GODAS products, the current ECCO route riverine
83 freshwater from land directly to the ocean by taking observed river runoff as seasonal climatology mass
84 flux over the top of several surface grid cells near the river mouths (Fekete et al. 2002; Stammer et
85 al.2004). Recent ECCO efforts have been extended to address the global-ocean estimates of pCO₂ and
86 air-sea carbon exchange (Carroll et al. 2020) and model resolution has been promoted as fine as 1-km
87 globally to investigate mesoscale-to-submesoscale dynamics in the open ocean (Su et al., 2018).
88 However, current ECCO is lack of representation of coastal interfaces and related feedbacks limiting
89 their predictability to global climate change, and may further impeding our ability to make informed
90 resource management decisions. In this study, we here improve the representation of river runoff in the
91 ECCO and systematically evaluate model performance in reproducing SSS within the vicinity of large
92 tropical and temperate river mouths. We also investigate the impact of runoff forcing, model grid
93 resolution, and grid type on coastal dynamics and critical physical properties near the plume regions. The
94 goal of this work is to provide a comprehensive sensitivity analysis of runoff forcing in multiple
95 simulations, which will aid in development of global ECCO that more robustly reflecting the Land-
96 Ocean-Aquatic-Continuum (LOAC).

97 The paper is organized as follows. Section 2 briefly introduces the ECCO model and the various
98 runoff forcing methods used in this study. Section 3 provides a comprehensive evaluation of model
99 sensitivity to horizontal grid resolution and river forcing. Section 4 discusses the sensitivity of plume
100 properties and coastal stratification. Results are summarized in Section 5.

101

102 **2 Methods**

103 **2.1 ECCO Simulations and Representation of River Runoff**

104 In this study, we employ the Massachusetts Institute of Technology general circulation model
105 (MITgcm; Marshall et al., 1997) in a number of model configurations that have been developed for the
106 ECCO project (Menemenlis et al., 2005; Forget et al., 2015; Zhang et al., 2018). The ECCO MITgcm
107 configurations that we use herein solve the hydrostatic, Boussinesq equations on either Cubed Sphere
108 (CS; Adcroft et al., 2004) or Latitude-Longitude-polar-Cap (LLC; Forget et al., 2015) grids. The cubed-



109 sphere configuration that we use is the so-called CS510 grid, which was developed for the ECCO2 project
110 (Menemenlis et al., 2008), consists of 6 faces with 510×510 dimension, and has quasi-homogeneous
111 horizontal grid spacing of 20 km. We also consider three different LLC grid configurations: LLC90,
112 LLC270, and LLC540, which have, respectively, 1° , $1/3^\circ$, and $1/6^\circ$ nominal horizontal grid spacing. The
113 LLC grids are aligned with lines of latitude and longitude between 70° S and 57° N, and locally
114 isotropic with grid spacing varying with latitude. In the tropics, the LLC grid is refined in the meridional
115 direction to better resolve zonal currents. At high latitudes, the LLC grid is adapted to a two-dimensional
116 conforming mapping algorithm for spherical geometry. For our experiments, we use LLC# horizontal
117 grids, where the # is the number of points along one-quarter of the Equator. Therefore, LLC90 means
118 360 grid points circle the equator. The model has 50 vertical z-levels; vertical resolution is 10 m in the
119 top 7 levels and telescopes to 450 m at depth. We use a third-order, direct-space-time (DST-3) advection
120 scheme, while vertical advection uses an implicit third-order upwind scheme. Vertical mixing is
121 parameterized using the GGL mixing-layer turbulence closure and convective adjustment scheme
122 (Gaspar et al., 1990). Lateral eddy viscosity in ECCOv4 is harmonic, with a coefficient of $0.005L^2/\Delta t$,
123 where L is the grid spacing in meters and $\Delta t = 3600s$. Depending on location, the resulting eddy
124 viscosity varies from $\sim 10^3$ to $\sim 1.6 \times 10^4 m^2s^{-1}$. Additional sources of dissipation in ECCOv4 are
125 from harmonic vertical viscosity and quadratic bottom drag, along with contributions from the vertical
126 mixing parameterization. A detailed description of ECCOv4 is provided in Forget et al. (2015).

127 ECCOv4 uses natural boundary conditions (Huang 1993; Roullet and Madec; 2000), in which
128 runoff is applied as a real freshwater flux forcing, which allows for material exchanges through the free
129 surface and more precise tracer conservation compared to virtual salt flux boundary conditions (Campin
130 et al., 2008). The model uses z^* rescaled height vertical coordinates (Adcroft and Campin, 2004) and
131 the vector-invariant form of the momentum equation (Adcroft et al., 2004). With z^* coordinates,
132 variability in free surface height is distributed vertically over all grid cells. For a water column that
133 extends from the bottom at $z = -H$ to the free surface at $z = \eta$, the z^* vertical coordinate is defined
134 as $z = \eta + s^*z^*$, where $s^* = 1 + \eta/H$ is the rescaling factor. The Boussinesq, depth-dependent
135 equations for conservation of volume and salinity under the vector-invariant form of the momentum
136 equations are:

137

138
$$\frac{1}{H} \frac{\partial \eta}{\partial t} + \nabla_{z^*} \cdot (s^* v) + \frac{\partial w}{\partial z^*} = s^* F \quad (1)$$



139
$$\frac{\partial(s^*S)}{\partial t} + \nabla_{z^*}(s^*Sv_{res}) + \frac{\partial(Sw_{res})}{\partial z^*} = s^*(D_{\sigma,S} + D_{v,S}) \quad (2)$$

140

141 where F is the surface freshwater flux (includes both precipitation minus evaporation and river runoff),
142 ∇_{z^*} is the gradient operator on z^* plane. S is the potential salinity, $D_{v,S}$ and $D_{\sigma,S}$ are subgrid-scale
143 vertical and along iso-neutral mixing, and v_{res} and w_{res} are the horizontal and vertical residual mean
144 velocity fields. Our daily, point-source runoff (DPR) experiments added freshwater to a single model
145 grid cell in the first vertical model layer, while the diffuse climatological runoff experiments added it
146 over multiple horizontal grid cells in the top layer. The amount of freshwater added to each model grid
147 cell decreased exponentially as a function of distance from river outlets.

148 2.2 Sensitivity Experiments

149 We first run five experiments, derived from the ECCOv4 set-up, to test the sensitivity of SSS in the
150 vicinity of large river mouths to ECCOv4 model grid resolution and runoff forcing (Table 1). The LLC90,
151 LLC270, and LLC540 corresponds to coarse ($1^\circ / \sim 100$ km), intermediate ($1/3^\circ / \sim 40$ km), and high
152 ($1/6^\circ / \sim 20$ km) resolution from low- to mid-latitudes. LLC90C and LLC270C are forced by monthly
153 climatological runoff from Fekete et al. (2002). The runoff has a spatial resolution of $\sim 1^\circ$ and has been
154 linearly interpolated to each grid cell. Therefore, runoff may be fluxed into a single grid cell in the coarse-
155 resolution run and over several grid cells in the high-resolution run. The twin experiments, LLC90R and
156 LLC270R, as well as the highest resolution run LLC540R, use Japanese 55-year atmospheric reanalysis
157 (JRA55-DO) river forcing dataset (Suzuki et al., 2017; Tsujino et al., 2018). JRA55-DO includes daily
158 river runoff is generated by running a global hydrodynamic model forced by adjusted land-surface runoff.
159 Comparing to the Fekete ECCOv4 runoff, JRA55-DO runoff has daily output; therefore, it can resolve
160 interannual variability and extreme floods and drought events. We add JRA55-DO runoff as point source
161 flux at a single grid cell adjacent to river outlets. In addition to the LLC grid, two additional experiments
162 are conducted on the widely-used cube-sphere ECCO2 grid to investigate model sensitivity to the choice
163 of grid topology (Table 1). CS510C is an ECCO2 run with monthly climatological runoff from Stammer
164 (2004). The Stammer runoff is spread over a pre-determined surface area in the vicinity of river mouths.
165 The spreading radius decreases exponentially with a 1000-km e-folding distance. Spatial fields of runoff
166 forcing for ECCOv4, ECCO2, and JRA55-DO are shown in Figure S1.

167

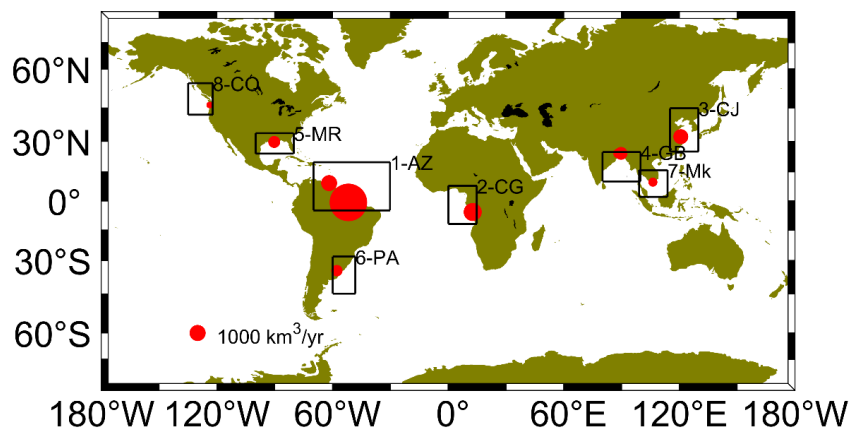
168



#	Experiment Name	Grid Type	Runoff Forcing	Grid spacing
1	LLC90C	Lat-Lon-Cap	ECCOv4 Climatology	55–110 km
2	LLC90R	Lat-Lon-Cap	JRA55-do	55–110 km
3	LLC270C	Lat-Lon-Cap	ECCOv4 Climatology	18–36 km
4	LLC270R	Lat-Lon-Cap	JRA55-do	18–36 km
5	LLC540R	Lat-Lon-Cap	JRA55-do	9–18 km
6	CS510C (Standard ECCO2)	Cube-sphere	ECCO2 Climatology	~19 km
7	CS510R	Cube-sphere	JRA55-do	~19 km

169 **Table 1:** Summary of all experiments. The ECCOv4 and ECCO2 climatological runoff is derived from
 170 Fekete et al. 2002 and Stammer et al. 2004, respectively. A comparison of runoff forcings is shown in
 171 Figure S1.
 172

173 Each sensitivity experiment is integrated for 26 years (1992–2017) and we analyze the final 3-year
 174 period (1 January 2015 to 31 December 2017). We begin our analysis in January 2015 because the high-
 175 resolution SMAP observations, which we use to evaluate model skill, are available from 1 April 2015.
 176 Ten large rivers at eight coastal regions spanning from low- to mid-latitudes are selected for detailed
 177 analysis; these include: the Amazon and Orinoco (AZ); Congo (CG), Changjiang (CJ), Ganges and
 178 Brahmaputra (GB), Mississippi (MR), Parana (PA), Mekong (MK), and Columbia (CO) rivers (**Figure**
 179 **1**).
 180



181 **Figure 1:** The 10 large rivers (red circles) in at 8 coastal regions (white boxes) used in our analysis:
 182 Amazon and Orinoco (South America, noted as region 1), Congo (Africa, region 2), Changjiang (Asia,
 183 region 3), Ganges and Brahmaputra (Asia, region 4), Mississippi (North America, region 5), Parana
 184 (South America, region 6), Mekong (Asia, region 7), Columbia (North America, region 8). Red circle
 185 size is scaled by the climatological river discharge magnitude.
 186

187
 188
 189



190 2.3 Target Diagram and Willmott Skill Score

191 The first part of our study compares the simulated salinity with the synchronized SMAP SSS
192 observations from 1 April 2015 to 31 December 2017. The level 3 SMAP version-3 SSS was produced
193 by the Jet Propulsion Laboratory (<ftp://podaac-ftp.jpl.nasa.gov> Yueh et al., 2013, 2014). We also
194 compare climatological SSS during this period with the World Ocean Atlas 2018
195 (<https://www.nodc.noaa.gov/OC5/woa18/>). For quantitative comparison, we use the Willmott skill score
196 (Willmott, 1981), a widely-used metric for quantifying agreement between models and observations. The
197 Willmott score is calculated as:

$$198 \quad W_{skill} = 1 - \frac{\sum_{i=1}^n (M_i - O_i)^2}{\sum_{i=1}^n (|M_i - \bar{O}| + |O_i - \bar{O}|)^2} \quad (3)$$

199 where M_i is the model estimate at t_i , O_i is the observation at time t_i , \bar{O} is the mean of the observations,
200 and n is the number of time records for comparison. Specifically, $W_{skill} = 1$ indicates perfect agreement
201 between model and observations; $W_{skill} = 0$ indicates that the model skill is equivalent to the
202 observational mean.

203 Furthermore, we conduct our skill assessment for model SSS on multiple experiments across several
204 regions. We also use Target diagrams (Jolliff et al. 2009) to efficiently visualize a suite of skill metrics.
205 Target diagrams are plotted in a Cartesian coordinate system with the x-axis representing the unbiased
206 root-mean-square-deviation (RMSD), the y-axis represents the bias, and the distance between the origin
207 and any point within the Cartesian space representing total RMSD.

$$208 \quad Bias = \frac{\sum_{i=1}^n (M_i - O_i)}{n} = \bar{M} - \bar{O} \quad (4)$$

$$209 \quad Unbiased \ RMSD = \sqrt{\frac{\sum_{i=1}^n [(M_i - \bar{M}) - (O_i - \bar{O})]^2}{n}} \quad (5)$$

$$210 \quad RMSD = \sqrt{\frac{\sum_{i=1}^n (M_i - O_i)^2}{n}} \quad (6)$$

211 \bar{M} represents the mean of the model estimates. These three skill assessment statistics are
212 particularly useful, as bias reports of the size of the model-observation discrepancies. Bias values near
213 zero indicate a close match, though it can be misleading as negative and positive discrepancies can cancel
214 each other. The unbiased RMSD removes the mean and is a pure measure of how model variability differs
215 from observational variability. The total RMSD provides an overall skill metric, as it includes
216 components for assessing both the mean (bias) and the variability (unbiased RMSD), i.e.,

$$217 \quad (Bias)^2 + (Unbiased \ RMSD)^2 = (RMSD)^2 \quad (7)$$



218 We normalize the bias, unbiased RMSD, and total RMSD by the observational standard deviation (σ_0)
219 to allow for the display of multiple experiment and regional SSS observations on a single Target Diagram.
220 According to the definition of unbiased RMSD, the value should always be positive. However, the $X <$
221 0 region of the Cartesian coordinate space may be utilized if the unbiased RMSD is multiplied by the
222 sign of the standard deviation difference (σ_d):

$$223 \quad \sigma_d = \text{sign}(\sigma_m - \sigma_o) \quad (11)$$

224 The resulting target diagram thus provides information about whether the model standard deviation is
225 larger ($X > 0$) or smaller ($X < 0$) than the observation's standard deviation, in addition to if the model
226 mean is larger ($Y > 0$) or smaller ($Y < 0$) than the observation's mean.

227 **2.4 Definition of plume characteristics**

228 We investigate the role of grid resolution and runoff forcing using several key metrics: plume area,
229 volume, and freshwater thickness. The plume area is defined as regions with SSS below a given salinity
230 threshold S_A . The freshwater volume, relative to the reference salinity, S_0 , is defined as the integral of
231 the freshwater fraction

$$232 \quad V_f(S_A) = \iiint_{s < S_A} \frac{S_0 - S(z)}{S_0} dV$$

233 where the volume integral is bounded by the isohaline S_A . Here, we assume the maximum salinity in
234 each selected region as the reference salinity S_0 . The freshwater thickness δ_{fw} represents the equivalent
235 depth of freshwater and is computed as:

$$237 \quad \delta_{fw} = \int_{-h}^{\eta} \frac{S_0 - S(z)}{S_0} dz$$

238
239 $S(z)$ is the depth-dependent diluted salinity due to the river discharge, η is the sea level, and h is the
240 bottom depth.

241 We also compute the freshwater flux along arcs (i.e., the edge of river mouth regions shown in
242 Figure S3). The freshwater flux is defined as:

$$243 \quad FW_{Trans} = \int_{x_1}^{x_2} \int_{-H}^{\eta} \frac{S_0 - S(z)}{S_0} v_n dx dz$$



244 where v_n is the velocity component normal to the arc (positive outward). $S(z)$ is the depth-dependent
245 diluted salinity; dz is the layer depth, and dx is the length of the cell. We interpolated the LLC270 and
246 LLC540 model results to the SMAP grid for unified dx and used the vertical cell depth from the model.

247 **3. Comparison with Observations**

248 We first estimate how the various ECCOv4 LLC simulations (Table 1) compare to observations in
249 the vicinity of 10 large river mouths. The synchronized SMAP SSS (01 April 2015 to 31 December 2017,
250 33-month) is used as the main verification dataset (Yueh et al., 2013, 2014). SMAP SSS has been
251 documented to exhibit bias compared to observed SSS in shallow waters near river mouths (Fournier et
252 al., 2017). Therefore, as an indication of absolute SSS, we also compare the model simulations to the
253 World Ocean Atlas 2018 (WOA18). We note that there may be relatively few observations incorporated
254 into the objectively-analysed WOA18 product near the coast, which may over-smooth salinity fronts.
255 Additionally, WOA18 is a 55-year climatology from 1955–2010; therefore, we can only compare model
256 climatology from 2015–2017. Overall, we use SMAP and WOA18 as “observational references”, where
257 our model-observation comparisons provide useful information on how SSS changes between
258 experiments rather than determine which experiment is closer to the real world.

259 The upper 10-m SSS biases relative to SMAP, averaged over the 33-month period, for CS510C
260 (standard ECCO2) as well as the LLC540R (highest resolution) are shown in Figure S2. Both SMAP and
261 WOA18 have $1/4^\circ$ horizontal grid resolution, therefore, we interpolated all model fields to this grid. For
262 both simulations, negative biases are found from low- to mid-latitudes, while positive biases occur at
263 high latitudes. When focusing on large river mouth regions (e.g. AZ, PA and CJ), the SSS bias is reduced
264 in LLC540R. This demonstrates that the choice of runoff forcing impacts on SSS at predominantly local
265 scales; however, background currents can transport the signal downstream or offshore to the open ocean
266 (Liu et al., 2009; Molleri et al., 2010).

267 Next, we compute mean model SSS near all selected river mouth regions, along with SMAP and
268 WOA18 (Table 2). The corresponding Willmott Skill (WS) numbers are listed in Table 3. We use the 1st
269 Empirical Orthogonal Function (EOF) derived from WOA18 to determine river mouth regions, since
270 WOA18 represents persistent low-salinity zones over the 30-year period. We remove the mean SSS field
271 before the EOF analysis. The 1st mode explains ~47–67% of the total variance. We then reconstruct the
272 dominant SSS anomaly field by multiplying the 1st PC with the spatial pattern. Locations with salinity
273 that is 1–2 PSU lower in the reconstructed SSS field is taken as the river mouth region, and all eight



274 regions are shown in Figure S3. Near the selected large river mouths, experiments with daily, point-
 275 source runoff forcing generally has lower SSS than experiments forced by climatological runoff
 276 (LLC90R vs. LLC90C; LLC270R vs. LLC270C; CS510R vs CS510C). Increasing model resolution
 277 generally results in regions becoming fresher (Table 2; LLC90C to LLC270C; LLC90R to LLC270R to
 278 LLC540R).
 279

River Mouth	Abb.	Discharge (m ³ /yr)	WOA 18	SMAP	LLC 90C	LLC 90R	LLC 270C	LLC 270R	LLC 540R	CS 510C	CS 510R
Amazon / Orinoco	AZ	6440	32.7	27.5	34.0	34.1	31.7	28.2	24.6	34.3	23.8
Congo	CG	1270	33.6	33.7	34.7	34.3	34.6	33.9	33.7	34.9	34.1
Changjiang	CJ	907	32.9	31.4	33.1	32.8	33.0	32.2	31.8	32.5	30.9
Ganges / Brahmaputra	GB	643	29.3	27.5	30.9	29.4	29.5	27.2	23.9	29.7	25.6
Mississippi	MR	552	33.5	34.8	35.8	34.7	35.8	34.1	33.8	35.3	34.1
Parana	PA	517	28.9	27.3	33.7	31.0	31.1	24.7	20.0	33.8	20.0
Mekong	MK	504	32.9	32.9	33.5	32.6	32.3	30.3	31.0	31.8	28.5
Columbia	CO	167	30.7	31.0	32.0	31.7	31.7	30.8	30.3	31.4	30.4

280 **Table 2:** The SSS near river mouth for WOA18, SMAP, and all experiments for the selected regions

281

282 An SSS comparison between SMAP and WOA18 showed no consistent patterns. Explaining
 283 differences between the two datasets is beyond the scope of this study; however, we acknowledge that
 284 some large differences complicate our comparison. Use of DPR forcing yielded higher W_{skill} scores in
 285 most regions when using SMAP as the observational reference, but not when using WOA18 (e.g.
 286 LLC270C/R for AZ, GB, MK). Additionally, a comparison to SMAP shows that W_{skill} scores become
 287 higher when model resolution increases from 1° to 1/3° (LLC90C vs LLC270C, LLC90R vs LLC270R),
 288 but lower when further increases to 1/6° (e.g. LLC270540R for Amazon, Ganges/Brahmaputra, Parana).
 289 In contrast, W_{skill} lacks consistency when comparing to WOA18 (e.g. at GB, W_{skill} associated with
 290 LLC90R exceeds that of both LLC270R and LLC540R). The higher or lower W_{skill} score is consistent
 291 with how much the model deviates from the observational reference. At the AZ region, SSS from
 292 LLC270R is less than 1 psu lower than the SMAP average, while LLC540R is roughly 3 psu lower.
 293 Therefore, LLC270R receives a skill score 0.92, higher than LLC540R (0.74). This also occurs with
 294 LLC270C and LLC270R when using WOA18 as the reference. For rivers in tropical and temperate zones,



295 the CS510 grid has a resolution comparable with the LLC540 grid, therefore, the SSS and skill scores
 296 are comparable between CS510R and LLC540R. Since the model grid type has a negligible impact on
 297 SSS for low- to mid-latitude rivers, we next focus on model sensitivity to grid resolutions.

298

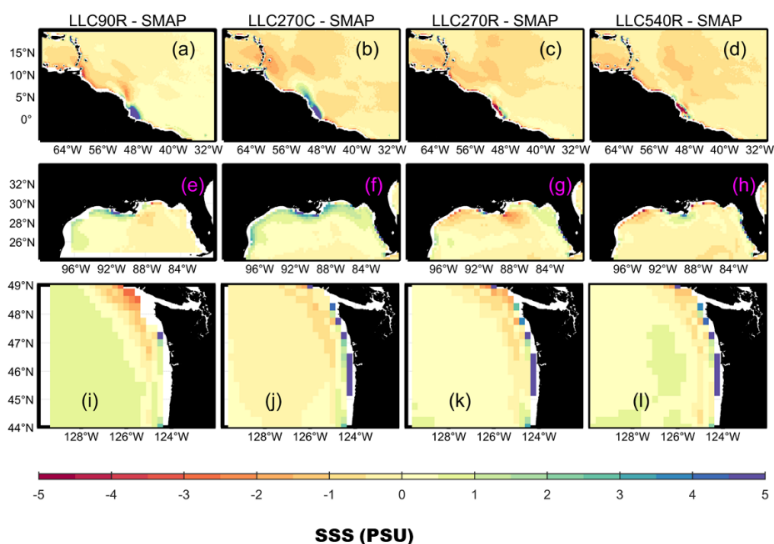
River Mouth	LLC90C	LLC90R	LLC270C	LLC270R	LLC540R	CS510C	CS510R
with SMAP							
Amazon / Orinoco	0.50	0.50	0.71	0.92	0.79	0.46	0.73
Congo	0.58	0.64	0.69	0.89	0.88	0.60	0.87
Changjiang	0.53	0.59	0.51	0.64	0.83	0.59	0.85
Ganges / Brahampura	0.61	0.71	0.69	0.85	0.69	0.57	0.70
Mississippi	0.55	0.79	0.53	0.77	0.75	0.49	0.72
Parana	0.37	0.51	0.45	0.62	0.40	0.37	0.40
Mekong	0.79	0.90	0.77	0.54	0.63	0.74	0.38
Columbia	0.46	0.60	0.49	0.73	0.74	0.27	0.61
with WOA							
Amazon / Orinoco	0.73	0.69	0.87	0.64	0.47	0.54	0.44
Congo	0.60	0.67	0.70	0.94	0.95	0.64	0.92
Changjiang	0.82	0.94	0.68	0.70	0.72	0.78	0.54
Ganges / Brahampura	0.72	0.90	0.92	0.78	0.51	0.73	0.59
Mississippi	0.46	0.59	0.46	0.68	0.73	0.49	0.66
Parana	0.40	0.45	0.45	0.42	0.29	0.40	0.29
Mekong	0.84	0.87	0.83	0.45	0.54	0.71	0.30
Columbia	0.51	0.62	0.63	0.87	0.84	0.51	0.90

299

300 **Table 3:** The Willmott skill score for each run as compared with WOA18 and SMAP. The river mouth
 301 was recognized by the 1st EOF of WOA18 (See Figures 5 and S1). Note that WOA18 data are a 30- year
 302 climatology (1981—2010) and not in the same period as SMAP and experiments.

303

304 To better compare the sensitivity of SSS to river forcing, we provide zoomed-in plots of the same
 305 comparison shown in Figure 1 for AZ, MR, and CO Rivers for all LLC simulations, representing large,
 306 medium, and small rivers (Figure 2). The positive bias is greatly reduced when applying daily, point-
 307 source river forcing, as well as increasing the horizontal grid resolution.



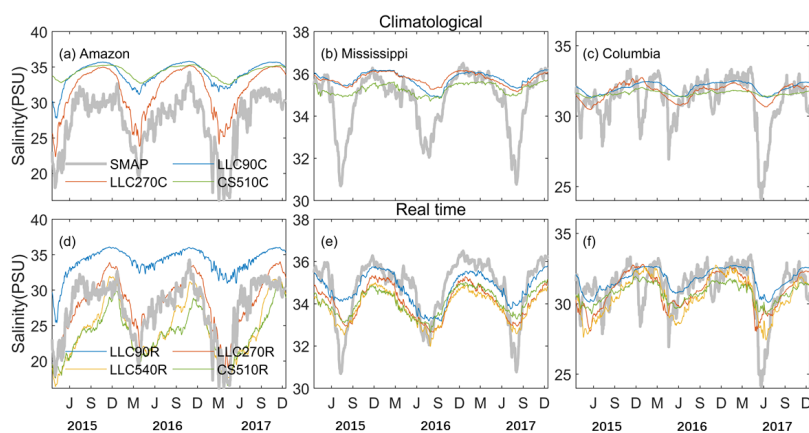
308

309 **Figure 2:** Zoomed-in view of SSS difference between model experiments and SMAP observations for
 310 large (Amazon, a–d), medium (Mississippi, e–h), and small (Columbia, i–l) rivers.

311 Timeseries for all LLC simulations and SMAP, at these three river mouths, are shown in **Figure 3**.

312 As in Figure 2, the bias decreases when daily, point-source river forcing is used and as the horizontal
 313 grid resolution increases. Additionally, there is substantial improvement in reproducing observed SSS
 314 variability. When using climatological runoff forcing, only seasonal variability is resolved in the
 315 simulations. When using DPR forcing, both the observed seasonal and interannual SSS variability are
 316 reproduced by the model. For example, the 2017 abnormally low SSS near the Amazon river mouth is
 317 associated with an extreme flooding event (Barichivich et al., 2018).
 318

319



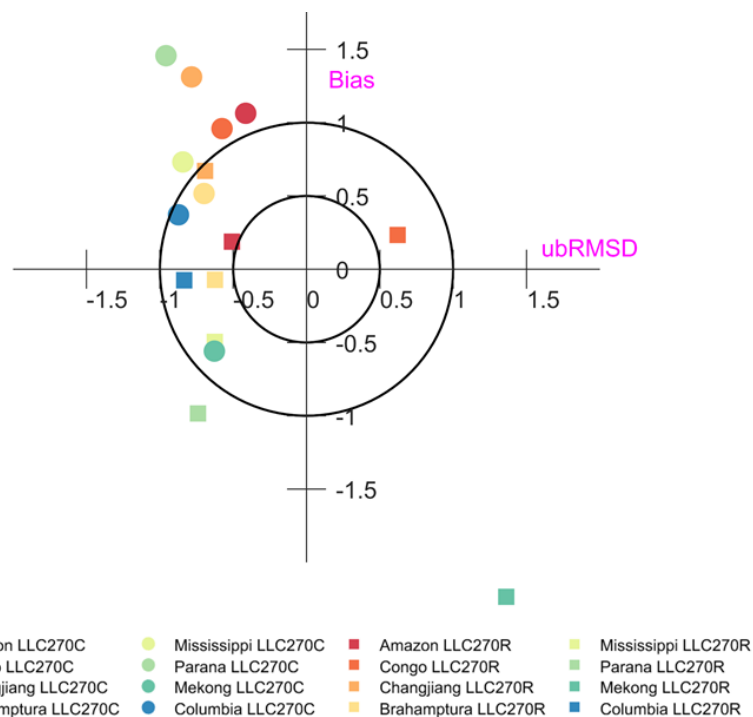
320



321 **Figure 3:** Areal averaged SSS in the Amazon, Mississippi and Columbia river mouth regions (see Figure
 322 S3) with climatological and daily, point-source runoff forcing for SMAP (thick gray line) and
 323 experiments (thin colored lines) with varying horizontal grid resolution. The method used to characterize
 324 the river mouth region is described in Section 3.

325
 326 Next, we quantify the difference in mean and variance between the SSS time series of LLC
 327 simulations and that of SMAP under different runoff forcing scenarios (**Figure 4**). The experiment with
 328 intermediate resolution shows that both the normalized bias and unbiased RMSD with daily forcing is
 329 lower than experiments with climatological forcing. Furthermore, using daily point-source runoff forcing
 330 results in mean simulated SSS that is closer to mean SMAP SSS in many regions (e.g. AZ, CG, GB, and
 331 CO). The total normalized RMSD improvements are primarily due to the normalized bias decrease. We
 332 find that most unbiased RMSD remains negative when varying the runoff forcing from climatological to
 333 daily. This implies that the variance of LLC simulations remains lower than SMAP observations as the
 334 runoff forcing changes. The only two exceptions are Congo and Mekong, possibly because JRA55DO
 335 runoff has stronger variability compared to the ECCOv4 climatology for the two rivers.

336

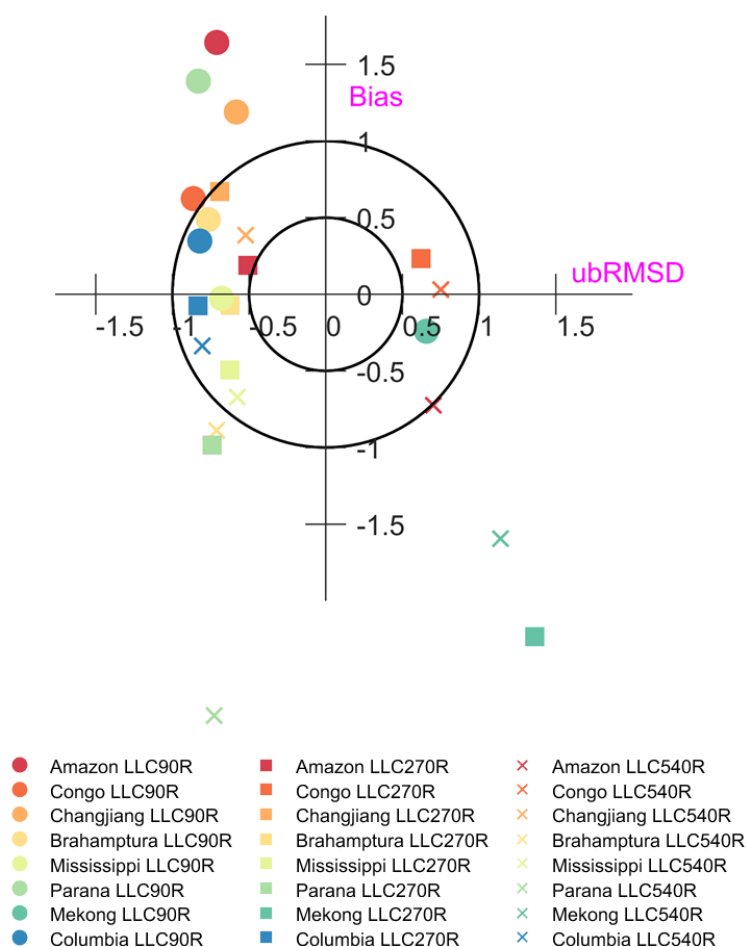


337
 338
 339
 340
 341

Figure 4: SSS target diagram near the selected river mouths (see Figure S3) for LLC270C and LLC270R simulations.



342 We also examine the bias and variance on the Target Diagram for experiments with varying
 343 grid resolution but similar daily runoff forcing (**Figure 5**). Our results show that the normalized bias
 344 decreases as the model resolution increases, while the unbiased RMSD decreases slightly with the sign
 345 remaining negative as the model resolution increases. This occurs everywhere, except for the two largest
 346 rivers (AZ and CG) where the sign becomes positive for LLC540R, indicating that the model variance
 347 exceeds the SMAP variance when using the high-resolution grid. In summary, the comparison with
 348 synchronized SMAP shows that using daily runoff and finer horizontal grid resolution improves the
 349 representation of SSS variability but at a cost of increased SSS bias.



350
 351 **Figure 5:** Same as Fig. 5, but for LLC90R, LLC270R, and LLC540R.

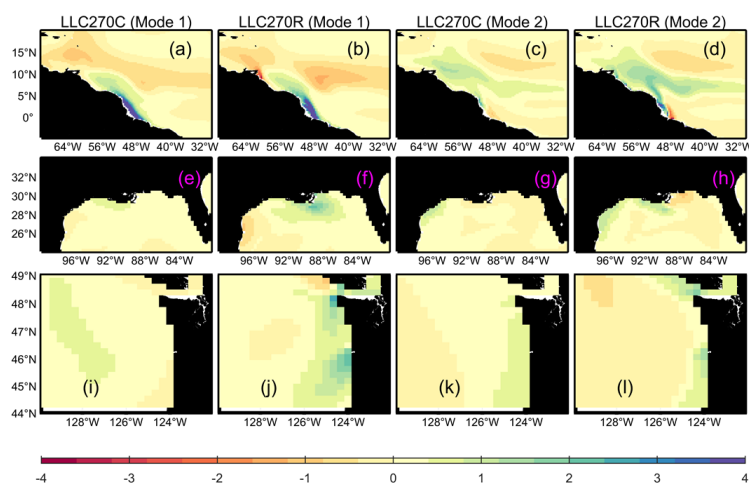


352 **4. Impact on River Plume Properties**

353 **4.1 EOF analysis of SSS**

354 We next investigate how model runoff improvements impact river plume properties such as plume
355 area, volume, and freshwater thickness. We first evaluate the plume SSS signature and dynamics through
356 EOFs; the mean is removed before the EOF analysis. The first and second mode of AZ, MR, and CO
357 using the same grid resolution but different runoff forcing is shown in Figures 6 and S4. The spatial
358 pattern reveals the salinity anomaly caused by the runoff, while the PC timeseries shows the timing. A
359 single value in spatial pattern or PC timeseries doesn't have a clear physical meaning, but together they
360 reveal how much salinity deviates from the mean. The PC timeseries for experiments with DPR forcing
361 clearly shows similar seasonal cycles, albeit with larger amplitudes and interannual variability.

362



363

364 **Figure 6:** 1st and 2nd EOF spatial patterns from the LLC270C and LLC270R simulations for the Amazon,
365 Mississippi, and Columbia rivers. The corresponding PC timeseries are normalized by the standard
366 deviation and multiplied back to the spatial mode.

367



368 For the AZ region, the LLC270R and LLC270C spatial patterns are similar for the first and second
369 mode. The first mode accounts for 59% (72%) of the total variance in LLC270R (LLC270C). The spatial
370 pattern reveals the presence of a low-salinity tongue; this is located in a narrow band along the
371 northeastern South American coast from February–June, which is associated with the large river
372 discharge and the northward-flowing Brazil Current. The second mode of LLC270R (LLC270C)
373 accounts for 33% (23%) of the total variance. The spatial pattern shows that the plume-like features
374 extend northwestward to the Caribbean Sea and Central Equatorial Atlantic Ocean from May–September.
375 This pattern is driven by Ekman currents associated with northeasterly wind stress, and the transport to
376 the Central Equator is due to the North Equatorial Counter Current (NECC, Lentz 1995a,b).

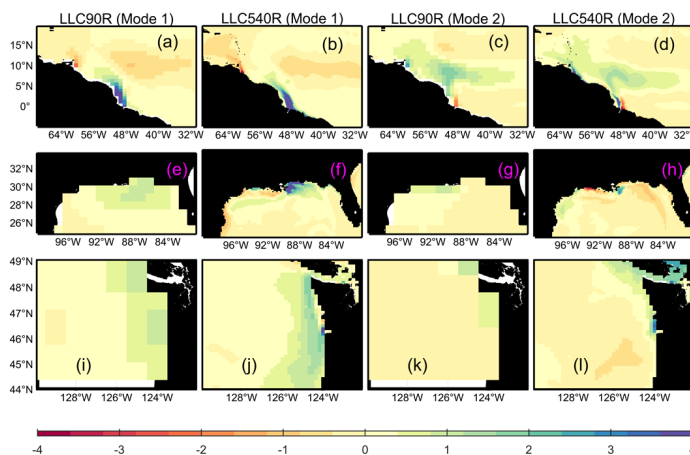
377 For the MR region, the first and second mode of LLC270R (LLC270C) explains 53% (66%) and
378 29% (18%) of the total variance, respectively. The spatial pattern of the first mode is generally similar.
379 There is a bulge-like plume feature that occupies a region near the MR mouth with a southeast extension
380 to the central Gulf of Mexico from May–October (Figure S4), while the freshwater signal in the vicinity
381 of the southeast MR mouth is stronger in LLC270R. The extension of low-salinity waters is due to the
382 upwelling favorable winds (southwesterly) from late-spring to summer, which transport the MR
383 freshwater offshore (Walker, 1996).

384 The first and second mode explains 63% (56%) and 29% (33%) of the variability at the CO region
385 in LLC270C (LLC270R), respectively. It has been previously recognized that the CO plume exhibits
386 seasonal variability forced by wind and freshwater discharge (*García Berdeal et al., 2002*). During winter,
387 Ekman transport resulting from the northward winds constrains the plume against the Washington coast.
388 Downwelling-favorable wind stresses strengthens the anti-cyclonic rotation of the river plume, resulting
389 in a coastally-attached winter plume. In contrast, prevailing southward wind stress results in offshore



390 Ekman transport; this advects the plume offshore, where it is influenced by the California Current over
391 long timescales and subsequently veers southward and offshore (Banas et al., 2009). This seasonal
392 pattern is shown in the first LLC270R mode and second LLC270C mode.

393 The first and second EOF modes for AZ, MR, and CO with daily runoff forcing in coarse (LLC90R)
394 and fine (LLC540R) grid resolution are shown in Figures 7 and S5. The plume-like features and
395 associated dynamics are similar to LLC270 in both runs. Additionally, the higher-resolution LLC540R
396 resolves fine-scale plume structure for a number of major rivers, which was previously revealed by
397 satellite observations, regional simulations, or neural network methods (e.g. meanders and rings of the
398 AZ plume due to the NBC retroreflection, Molleri et al. 2010); “horseshoe” patterns of the MR plume
399 associated with Texas floods (Fournier et al. 2016), and the bidirectional CO plume during variable
400 summer wind patterns (Liu et al. 2009). Overall, EOF SSS analysis shows that general plume pattern and
401 dynamics are grid independent; however, fine-scale plume structures are only resolved by high-
402 resolution simulations.



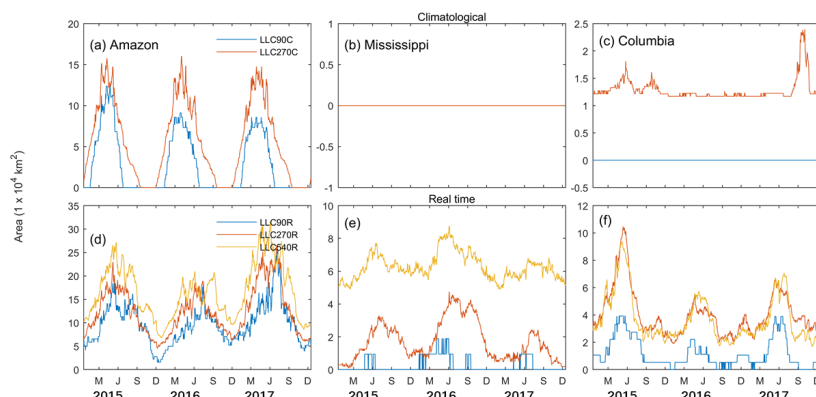
403
404 **Figure 7:** Same as Fig. 6 but for the LLC90R and LLC540R simulations. The corresponding PC
405 timeseries are normalized by the standard deviation and multiplied back to the spatial mode shown in
406 Figure S5.

407



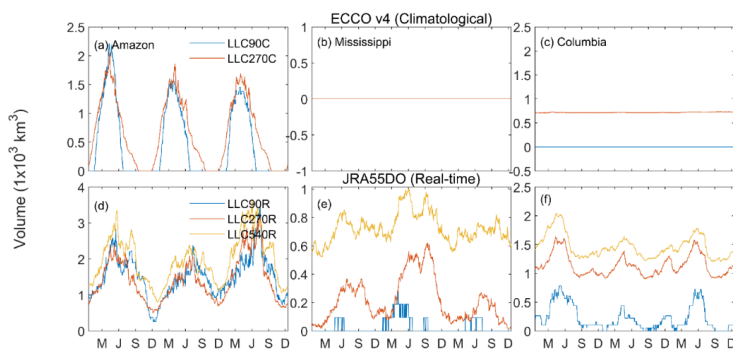
408 4.2 Plume Area, Volume, Freshwater Thickness, and Transport

409 We first calculated plume area using a salinity threshold from 28 to 36 PSU (Figure S6). The
410 absolute plume area varied with the choice of S_A . Since the seasonal and interannual variability are
411 comparable once the plume can be clearly resolved at the given threshold, we only show the plume area
412 within $S_A = 30$ psu under the climatological and daily runoff forcing at the coarse, intermediate, and
413 high resolution runs (Figure 8). Figure 9 presents a time series of freshwater volume within the given
414 salinity during this period. There is a stronger interannual variability when using DPR, along with larger
415 plume area and volume during flood years. The MR and CO plume area/volume cannot be explicitly
416 resolved at the $S_A = 30$ threshold when using the climatological and runoff forcing since river runoff
417 has been distributed over a broad spatial grids and surface salinity decrease is small. For the AZ region,
418 the averaged plume area (volume) approaches 6×10^4 km² (7×10^2 km³) in LLC270C, whereas it is
419 only about 3×10^4 km² (5×10^2 km³) in LLC90C. In contrast, the MR and CO plume area (volume)
420 is easily recognized when using DPR forcing. The AZ plume increases as the grid resolution increases,
421 reaching 10, 13, and 17×10^4 km² in LLC90R, LLC270R, and LLC540R, respectively. The freshwater
422 volume in coarse-, intermediate-, and high-resolution runs is comparable, with values of $\sim 1.5 - 2 \times 10^2$
423 km³. The plume area and volume in the MR region is more sensitive to the model grid resolution than
424 AZ and CO. The LLC540R plume area is $\sim 3-4$ times higher than LLC270R, while LLC270R is $\sim 6-7$
425 times higher than LLC90R. For the CO region, the plume area when using DPR forcing is similar
426 between intermediate- and fine-resolution experiments, with the area in LLC270R and LLC540R
427 increasing to $\sim 1 \times 10^5$ km² during the 2015 flood year. In contrast, LLC540R maintains a larger plume
428 volume than the intermediate resolution run.



429
 430 **Figure 8:** Same as Fig. 7 but for the LLC90R and LLC540R simulations. The corresponding PC
 431 timeseries are normalized by the standard deviation and multiplied back to the spatial mode shown in
 432 Figure S5.

433

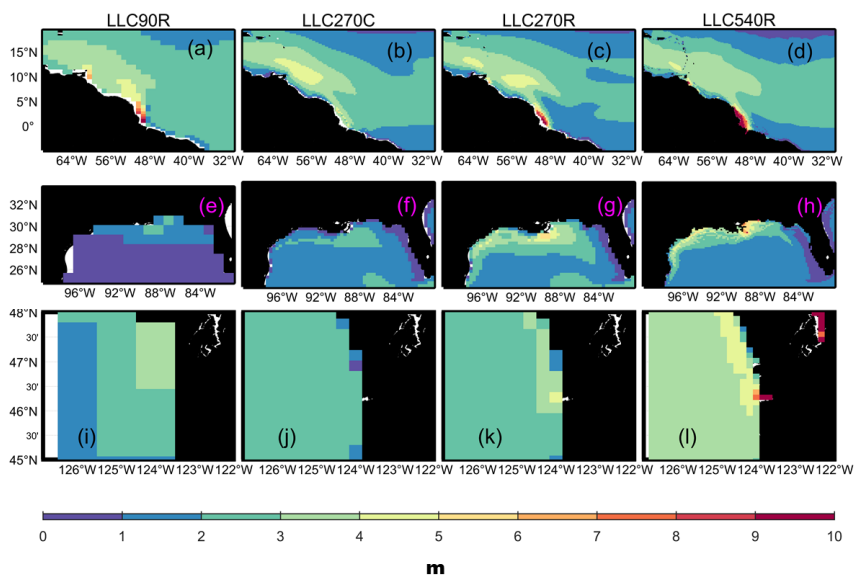


434
 435 **Figure 9:** Freshwater volume within 30 PSU for the Amazon, Mississippi, and Columbia river regions
 436 for various experiments, reference salinity is 36 PSU.

437 The sensitivity of plume area and volume to runoff forcing and grid resolution reflects the
 438 experiments ability to resolve the horizontal advection and downward mixing of riverine freshwater. This
 439 can be partially reflected in the freshwater thickness calculation, which is shown in Figure 10. For the
 440 intermediate resolution experiments, the maximum freshwater thickness δ_{fw} is over 10 m, 5 m, and 4 m
 441 near the AZ, MR, and CO river mouths when using DPR, as opposed to 4 m, 2 m, and 2 m, when using
 442 climatological runoff. Additionally, the freshwater thickness in experiments with DPR but different grid
 443 resolutions (LLC270R and LLC540R) demonstrates that a coherent plume rotates and responds to



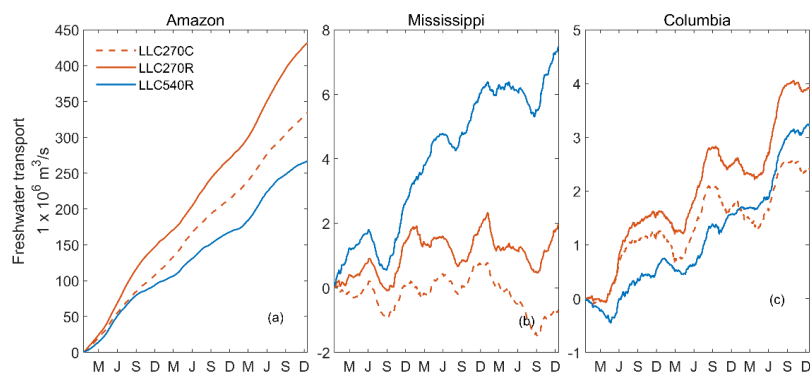
444 external wind and background flows; this coastal plume structure is largely absent in the coarser LLC90R.
445 The coarse resolution experiment exhibits a more diffuse response, with low salinity near MR and CO
446 river mouths. Note that the runoff forcing is identical between LLC90R, LLC270R, and LLC540R
447 experiments, and differences in plume area, volume, and freshwater thickness are due to model resolution
448 alone. The freshwater flux in the higher resolution experiments can result in larger inflow velocities, a
449 stronger baroclinic response, and consequently a more vigorous coastal plume. The plume area and
450 volume in MR region is more sensitive to grid resolution — this possibly results from the representation
451 of shelf bathymetry. The Texas-Louisiana shelf is wider and shoals more gradually from the coastline
452 compared to the northern Brazilian shelf (AZ) and Washington shelf (CO). When adding the same
453 amount of freshwater in shallow water regions, high resolution experiments generate a larger pressure
454 gradient force than the intermediate resolution, which drive a stronger baroclinic effect and elevate
455 coastal currents. The alongshore currents can advect the MR Plume water downcoast, enlarging the
456 plume area. Besides, the plume waters may be entrained downward by strong sub-grid vertical mixing
457 and adjustment, e.g. meso-scale eddies, when flowing offshore to the open ocean as the horizontal
458 resolution increases from intermediate to high. The eddies in high resolution run at AZ and CR may
459 break up the plumes, shrinking the area comparing to low-to-intermediate resolution run (Figure S6).



460

461 **Figure 10:** Freshwater thickness for LLC90R, LLC270C, LLC270R, and LLC540R experiments.

462 The integrated freshwater transport is shown in Figure 11. The coarse-resolution LLC90 simulation
 463 does not resolve the selected arc and therefore is not shown. For the LLC270 simulation, the integrated
 464 freshwater transport when using the climatological runoff is smaller than when using DPR in the AZ,
 465 MR, and CO regions. When further increasing model resolution to LLC540, FW_{Trans} only increases at
 466 the MR region, but not in the AZ and CO regions, which is consistent with the plume area/volume
 467 response. The larger freshwater transport at the MR region is mainly due to a strengthening of the coastal
 468 current along the shallow continental shelf. We note that these results may vary depending on the choice
 469 of arc. Additionally, further increases in the model grid resolution may distort the plume characteristic
 470 and lead to different conclusions. Again, this similarity suggests that the baroclinic current becomes
 471 stronger as model grid resolution increases in shallower and wider shelf regions.



472

473 **Figure 11:** Integrated freshwater transport from 2015–2017 along the arc of the Amazon, Mississippi,
474 and Columbia river mouth. Arc is defined as the edge of the river mouth region shown in Figure S3.

475

476 4.3 Impact on Ocean Properties Associated with SSS

477

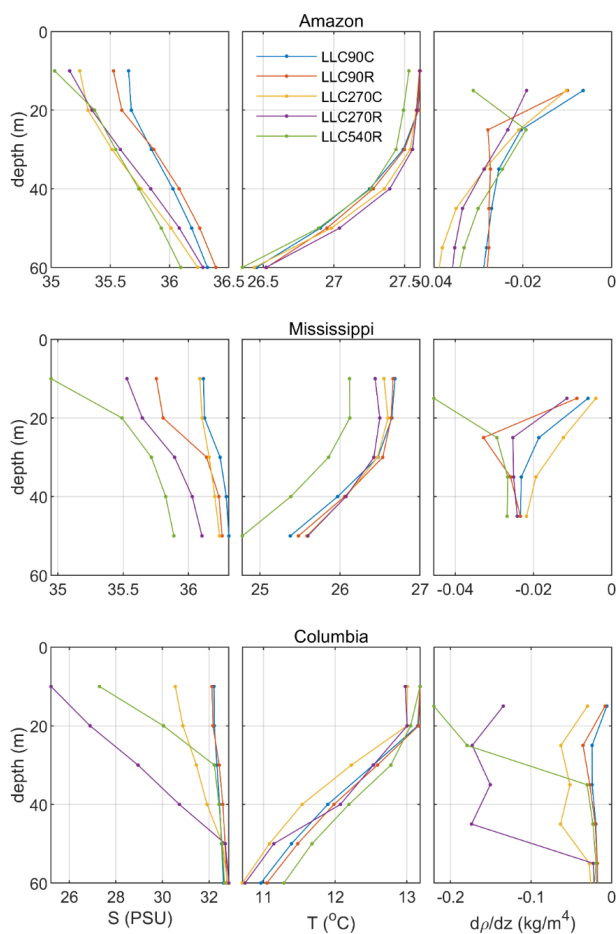
478 In this section, we examine the sensitivity of stratification and mixed layer depth (MLD) between
479 different experiments. Figure 12 shows 3-year averaged vertical profiles of salinity, temperature, vertical
480 density gradient dp/dz (ρ is the potential density) near the AZ (top), MR (middle), and CO (bottom)
481 river mouths, respectively. The profiles are averaged over the horizontal regions shown in Figure S3.
482 The vertical density gradient is an important indicator of stratification strength. The salinity differences
483 between climatological (LLC90/270C) and DPR forcing (LLC90/270R) are large near the surface and
484 diminish with increasing depth. The temperature difference when using the two type of runoff forcing is
485 insignificant, demonstrating that the stratification is primarily determined by salinity and the addition of
486 freshwater. Additionally, DPR forcing greatly increases subsurface stratification, which implies a
487 decrease in vertical mixing.

487

488 Figure 12 also shows sensitivity of upper-ocean stratification to various model grid resolutions.
489 The profiles show a significant decrease in salinity from the surface to 50-m depth as the resolution



489 increases, which impacts the stratification (rightmost panels). We note that the vertical density gradient
490 has a subsurface maximum in the coarse- and intermediate-resolution run, while the high-resolution
491 experiment has a surface maximum due to low-salinity water concentrated in the surface level. SST is
492 highest in LL540R at AZ and MR, reflecting that heat is preserved at the surface due to the increase in
493 subsurface stratification.

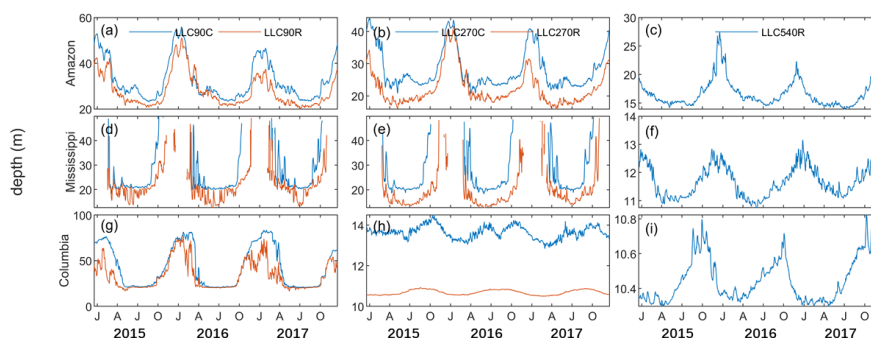


494
495 **Figure 12:** Mean 3-year (2015-2017) salinity, potential temperature, and vertical density gradient
496 ($d\rho/dz$) profiles.

497



508 The sensitivity of stratification in the above analysis implies that the MLD can be altered by river
509 forcing and grid resolution. We compare the MLD in the vicinity of AZ, MR, and CO during the
510 simulation period in Figure 13. The MLD in our calculation uses the threshold method, in which deeper
511 levels are examined until one is found with density differing from the near surface by more than 0.03
512 kg/m^3 (de Boyer Montégut et al., 2004). This reflects the maximum depth of the boundary layer that is
513 sustained by riverine freshwater. Interestingly, all experiments simulate the annual cycle of MLD. There
514 was relatively shallow MLD from April to December, which corresponds to periods of high river
515 discharge. The MLD in the DPR forcing and high-resolution scenario is shallower than the climatological,
516 low-resolution scenario, which is consistent with vertical salinity and stratification profiles shown in
517 Figure 11.



508 **Figure 13.** 2015–2017 daily MLD, averaged in the vicinity of the Amazon River (upper panels),
509 Mississippi River (middle panels), and Columbia River (lower panels) mouth. MLD is computed based
510 on de Boyer Montegut et al. (2004).
511

512

513 5. Discussion and conclusions

514 In this study, we investigate the model sensitivity of runoff forcing and grid resolution and type
515 under the ECCO framework. We find that DPR greatly improves model representation of global rivers,
516 with horizontal model resolution having a substantial control on SSS in the vicinity of river mouths. We



517 observe no major changes in tropical and temperate river mouth SSS when using cube sphere grid or
518 LLC grid types when using the same river forcing. A comparison with synchronized SMAP observations
519 shows that the use of DPR forcing and intermediate grid resolution can increase the model performance
520 in simulating SSS in the vicinity of river mouths. However, further increasing model grid resolution from
521 intermediate to high may result in an additional SSS bias towards fresher values.

522 Previous theoretical modelling studies have demonstrated that, in the absence of external forcing,
523 large river plumes influenced by rotational effects tend to veer anticyclonically and form a bulge region
524 near the river mouth as well as an along-shore downstream coastal current as Kelvin waves (Kourafalou
525 et al. 1996; Yankovsky and Chapman, 1997). Additionally, idealized numerical simulations have
526 revealed that river plume behaviour is greatly impacted by external forcing. Chao (1988a, b)
527 demonstrated that vertical mixing, bottom drag, and bottom slope greatly impact the spin-up,
528 maintenance, and dissipation of river plumes. Fong and Geyer (2001) revealed that a surface-trapped
529 river plume would thin and be advected offshore by cross-shore Ekman transport. Fong and Geyer (2002)
530 suggested that the ambient current, which is in the same direction as the geostrophic coastal current, can
531 augment plume transport. Our ECCO experiments are examining the above river plume dynamic theory
532 globally with realistic topography and external atmospheric forcing. Our EOF analysis of SSS at the AZ,
533 MR, and CO shelves show that the general spatial and temporal patterns plume related to river discharge,
534 wind, and currents are independent of the grid resolutions and forcing formulations examined in this
535 study, which are quite consistent with those previous studies. However, higher resolution and DPR
536 forcing may be particularly important for resolving the fine-scale plume dynamics for small rivers. Using
537 DPR forcing and increasing the model grid resolution from coarse to intermediate increases the river
538 plume area, volume, and freshwater transport, while further increasing the model resolution from



539 intermediate to high has mostly regional effects. Shallow and wide shelf regions, such as the Mississippi
540 Delta, are more sensitive compared to AZ and CO. This suggests high resolution model may take more
541 computational resources without promoting the spatiotemporal scales of interest system dynamics. Two
542 potential solutions are applying domain nesting scheme and spatially variable model adapting the global-
543 scale open ocean (~ km) and small-scale coastal and estuarine environments (~ m).

544 We also found that using DPR forcing and increasing the model grid resolution can stabilize the
545 water column at subsurface and shoal the MLD. This may have significant implications for
546 biogeochemical cycles and air-sea exchange in coastal zones. From the biogeochemistry perspective,
547 freshwater introduced by the river increase shelf stratification, preventing the reoxygenation of bottom
548 waters and thus may generate large hypoxic regions (Fennel, et al. 2011; Feng et al. 2019). From the air-
549 sea interaction perspective, on one hand, SST can trigger deep atmospheric convection and strong rainfall.
550 On the other hand, strong near-surface stratification may inhibit cooling and intensify tropical cyclones
551 (Cione and Uhlhorn, 2003; Neetu et al., 2012; Rao and Sivakumar, 2003; Sengupta et al., 2008; Vialard
552 & Allison et al., 2000; Vinaychandran et al., 2002). We envision that future work investigating river
553 impacts on ocean-atmospheric and earth system dynamics could be accomplished by coupling our
554 improved ECCO simulations with an atmospheric general circulation model (AGCM).

555 In the state-of-art OGCMs, ESMs, and most GODAS products, river runoff is incorporated on coarse
556 resolution grids as augmented precipitation. Climatological runoff forcing is often used in conjunction
557 with artificial spreading, along with a virtual salt flux scheme. Tseng et al. (2016) examined model
558 sensitivity to the spreading radius, turbulent mixing parameterization, reference salinity, and vertical
559 distribution of riverine freshwater on 1° resolution in Community Earth System Model (CESM). For all
560 factors examined, they found that the model results are most sensitive to the spreading radius, which



561 substantiates the importance of our finding that the associated plume properties including the area hence
562 the SSS near river mouths exhibit strong responses when switching the runoff flux from diffusive
563 climatological to daily point-source.

564 The present state-of-the art regional scale estuarine models can simulate estuarine hydrodynamics
565 and biogeochemical processes in a robust manner. The inlet approach, which defines a rectangular breach
566 in coastal land cells with uniform density and discharge, is widely used (Herzfeld, 2015; Garvine, 2001).
567 An additional barotropic pressure term may be added to account for pressure gradients induced by the
568 freshwater plume (Schiller and Kourafalou, 2011). The inlet approach has also been used in global z-
569 coordinate models by injecting freshwater in multiple vertical grid cells (Griffies et al. 2005). In our
570 simulations, changes in sea level are redistributed over all vertical grid cells by the rescaled height
571 vertical coordinate. This is similar to the inlet approach in the regional models, which add a mass or
572 volume flux of freshwater to a breach in coastal land cells (Garvine 1999). Herzfeld (2015) investigated
573 the role of model resolution on plume response at the Great Barrier Reef (GBR) using the Regional
574 Ocean Modeling System (ROMS). The study found that the plume veered left and followed a northward
575 trajectory to Cape Bowling Green in a 1 km resolution model but not in a 4 km resolution model. Our
576 findings are consistent with this result; plume properties in our intermediate resolution simulations are
577 more clearly detected than in the coarse resolution simulations. In addition, our results expand on their
578 findings by showing that the sensitivity of plume properties and freshwater transport in high resolution
579 model are highly-dependent on shelf bathymetry. Schiller and Kourafalou (2010) investigated the
580 dynamics of large-scale river plumes in idealized numerical experiments using HYCOM to address how
581 the development and structure of a buoyant plume is affected by the vertical and horizontal redistribution
582 of river inflow and bottom topography. Their experiments show that a narrow inlet, flat bottom facilitates



583 a larger right-turning plume bulge region compared to a wide inlet, slope bottom (see their Figure 8
584 Riv2c-f, Riv2c-s). This is complementary to our findings that the MR plume, located on the wide and
585 shallow LA shelf, has a larger horizontal plume area compared to the AZ and CO plume when increasing
586 the horizontal resolution from intermediate to high. However, their discussion was limited to an idealized,
587 rectangular model domain without external forcing, while our model simulations provide a realistic
588 application to natural river plume systems. The global application of the regional inlet representation of
589 river forcing was also used by NOAA's Geophysical Fluid Dynamics Laboratory (GFDL) models
590 (Griffies et al., 2005). An internal, pre-computed salinity source term was introduced into multiple
591 vertical layers. However, river representation was done through VSF rather than through real mass or
592 freshwater volume flux. Adding the real volume and mass of freshwater through multiple layers has been
593 widely used in regional models like ROMS; it may be useful to adapt this technology into future ECCO
594 simulations and comparing the results with the current surface injection methods.

595 For the global ocean, river runoff is much smaller than the precipitation and evaporation flux;
596 therefore, for most OGCMs, ESMs, and GODAS products it is parameterized. One of the most significant
597 expected signatures of global warming is an acceleration of the terrestrial hydrological cycle (IPCCs,
598 2019; Piecuch and Wadehra, 2020). Both can significantly affect the magnitude, distribution, and timing
599 of global runoff, leading to extremes in the frequency and magnitude of floods and droughts. When
600 considering issues related to water resource management under climate and land use/land cover change,
601 key question such as "how will coastal oceans be impacted from flood and drought events?" is
602 challenging to answer (Fournier et al. 2019). In the future, high-resolution global-ocean circulation
603 models with DPR forcing may help identify the primary forcing mechanisms (such as those from climate-



604 driven extreme events) that drive spatiotemporal variability of large river plume systems just as skillfully
605 as regional model set-ups.

606 Improved model representation of rivers may not be as important for global or basin- scale
607 hydrological cycles as precipitation and evaporation (Du and Zhang, 2015), but may be critical for the
608 global carbon cycle (Friedlingstein et al., 2019; Resplandy et al. 2018). River delivers large amounts of
609 anthropogenic nutrients to the coastal zone (Seitzinger et al., 2005, 2010). The autochthonous production
610 will transform inorganic nutrients to organic while sequestering atmospheric CO₂. More importantly,
611 rivers also deliver dissolved organic carbon (DOC) and particulate organic carbon (POC) to the coastal
612 ocean, which can be remineralized and released as CO₂ to the atmosphere. Until recently, most global-
613 ocean biogeochemistry models omitted or poorly represented riverine point sources of nutrients and
614 carbon. Lacroix et al. 2020 added yearly-constant riverine loads to the ocean surface layer on coarse
615 resolution (1.5°) model and assessed that CO₂ outgassing from river loads accounted for ~10% of the
616 global ocean CO₂ sink. We anticipate that the implementation of DPR forcing and higher-resolution grids
617 in ESMs and the ECCO biogeochemical state estimates (ECCO-Darwin, Carroll et al., 2020) will help
618 better resolve the global carbon budget (Friedlingstein et al., 2019).

619 LOAC development has historically had a low priority in OGCMs, ESMs, and GODAPs and
620 exchange of freshwater between rivers/estuaries and the coastal ocean has been previously neglected.
621 Our results demonstrate that the representation of runoff forcing in ECCO simulations is a major source
622 of bias for coastal SSS. We believed our improvements of river runoff in ECCO will directly contribute
623 to: (i) the evaluation, understanding, and improvement of river-dominated coastal margins in global-
624 ocean circulation models, (ii) investigation of mechanisms that drive seasonal and interannual variability
625 in coastal plume processes, and (iii) bridging the gap between land-ocean interactions. These efforts will



626 ultimately help to better resolve land-ocean-atmosphere processes and feedbacks in next-generation earth
627 system models.

628 **Code and Data Availability**

629 The MITgcm and user manual are available from the project website: <http://mitgcm.org/>. The ECCOv4
630 setup can be found at http://wwwcvs.mitgcm.org/viewvc/MITgcm/MITgcm_contrib/llc_hires/. The
631 exact version of MITgcm, ECCOv4 configuration, MATLAB routines to process the ECCOv4 output,
632 generate the target model skill assessment diagram, and produce the paper figures are archived on Zenodo
633 (doi:10.5281/zenodo.4106405). The SMAP observations can be downloaded from
634 <http://apdrc.soest.hawaii.edu/las/v6/dataset?catitem=2928>. The model forcing and simulated salinity
635 fields at different resolutions are archived on Zenodo (doi:10.5281/zenodo.4095613)

636

637 **Author Contribution**

638 Dimitris Menemenlis designed the experiments and Hong Zhang carried them out. Yang Feng, Dimitris
639 Menemenlis, Dustin Carroll developed the model code and performed the simulations. Yang Feng
640 prepared the manuscript with contributions from Huijie Xue, Dustin Carrol, Yan Du, and Hui Wu

641

642 **Acknowledgment**

643 The work was supported by CAS Pioneer Hundred Talents Program Startup Fund (Y9SL11001);
644 Southern Marine Science and Engineering Guangdong Laboratory (Guangzhou) (GML2019ZD0303,
645 2019BT2H594), ISEE2018PY05 from Chinese Academy of Sciences; the Chinese Academy of
646 Sciences (XDA15020901; 133244KYSB20190031), and Guangdong Key Laboratory of Ocean Remote
647 Sensing (South China Sea Institute of Oceanology Chinese Academy of Sciences) (2017B030301005-
648 LORS2001). D.M., D.C., and H.Z., carried out research at Jet Propulsion Laboratory, California
649 Institute of Technology, under contract with NASA, with grants from Biological Diversity, Physical
650 Oceanography, and Modeling, Analysis, and Prediction Programs.

651

652



653 **References**

- 654 Adcroft, A., and Campin, J.-M., Rescaled height coordinates for accurate representation of free-surface
655 flows in ocean circulation models, *Ocean Modelling*, 7(3), 269-284,
656 doi:10.1016/j.ocemod.2003.09.003, 2004
- 657 Adcroft, A., Campin, J.-M. Hill, C. and Marshall, J., Implementation of an Atmosphere–Ocean General
658 Circulation Model on the Expanded Spherical Cube, *Monthly Weather Review*, 132(12), 2845-2863,
659 doi:10.1175/MWR2823.1, 2004
- 660 Banas, N. S., MacCready, P. and Hickey, B. M., The Columbia River plume as cross-shelf exporter and
661 along-coast barrier, *Continental Shelf Research*, 29(1), 292-301, doi:10.1016/j.csr.2008.03.011.,2009
- 662 Barichivich, J., Gloor, E., Peylin, P., Brienen, R. J. W., Schöngart, J., Espinoza, J. C., and Pattnayak,
663 K. C., Recent intensification of Amazon flooding extremes driven by strengthened Walker circulation,
664 *Science Advances*, 4(9), eaat8785, doi:10.1126/sciadv.aat8785.,2018
- 665 Bentsen, M., The Norwegian Earth System Model, NorESM1-M - Part 1: Description and basic
666 evaluation of the physical climate, *Geoscientific. Model Development*, 6, 687-720, doi:10.5194/gmd-6-
667 687-2013.,2013
- 668 Bourgeois, T., Resplandy, J. C. Orr, L., Terhaar, J., Ethé, C., Gehlen, M. and Bopp, L., Coastal-ocean
669 uptake of anthropogenic carbon, *Biogeosciences*, 13(14), 4167-4185, doi:10.5194/bg-13-4167-
670 2016.,2016
- 671 Campin, J.-M., Marshall, J. and Ferreira, D., Sea ice–ocean coupling using a rescaled vertical
672 coordinate z^* , *Ocean Modelling*, 24, 1-14, doi:10.1016/j.ocemod.2008.05.005., 2008
- 673 Carroll, D., Menemenlis, Adkins, J.F., Bowman, K.W., Brix, H., Dutkiewicz, S., Gierach, M. M., Hill,
674 C., Jahn, O., Landschützer, P., Lauderdale, J. Liu, J.M., Naviaux, J.D., Manizza, M., Rödenbeck,
675 C., Schimel, D. S., Van der Stocken, T., and Zhang, (2020) H, Seasonal to Multi-decadal Air-sea CO₂
676 Fluxes from the Data-constrained ECCO-Darwin Global Ocean Biogeochemistry Model, *Journal of*
677 *Advances in Modeling Earth Systems*, Accepted
- 678 Chao, S. -Y., River-forced estuarine plumes. *Journal of Physical Oceanography.*, 18, 72 – 88.
679 [doi:10.1175/1520-0485\(1988\)018<0072:RFEP>2.0.CO;2](https://doi.org/10.1175/1520-0485(1988)018<0072:RFEP>2.0.CO;2), 1988
- 680 Chao, S. -Y., Wind-driven motion of estuarine plumes, *Journal of Physical Oceanography*, 18, 1144-
681 1166. doi:10.1175/1520-0485(1988)018<1144:WDMOEP>2.0.CO;2; 1988
- 682 Cione, J. J., and Uhlhorn, E. W. Sea surface temperature variability in hurricanes: Implications with
683 respect to intensity change. *Monthly Weather Review*. 1783-1796, doi:10.1175/2562.1; 2003



- 684 de Boyer Montégut, C., Madec, G., Fischer, A. S., Lazar, A. & Ludicone, D, Mixed layer depth over
685 the global ocean: An examination of profile data and a profile-based climatology, 109(C12),
686 doi:10.1029/2004jc002378.,2004
- 687 Denamiel, C., Budgell, W. P. & Toumi, R, The Congo River plume: Impact of the forcing on the far-
688 field and near-field dynamics, Journal of Geophysical Research-Oceans, 118, 964–989,
689 doi:10.1002/jgrc.20062.,2013
- 690 Du, Y., & Zhang, Y., Satellite and Argo Observed Surface Salinity Variations in the Tropical Indian
691 Ocean and Their Association with the Indian Ocean Dipole Mode. J. Climate, 28, 695–713,
692 doi:10.1175/JCLI-D-14-00435.1.,2015
- 693 Fekete, B. M., Vörösmarty, C. J. and Grabs, W, High-resolution fields of global runoff combining
694 observed river discharge and simulated water balances, 16(3), 15-11-15-10,
695 doi:10.1029/1999gb001254.,2002
- 696 Fennel, K., et al. Carbon cycling in the North American coastal ocean: a synthesis, Biogeosciences,
697 16(6), 1281-1304, doi:10.5194/bg-16-1281-2019.,2019
- 698 Fennel, K., Hu, J., Laurent, A., Marta-Almeida, M., & Hetland, R. Sensitivity of hypoxia predictions
699 for the northern Gulf of Mexico to sediment oxygen consumption and model nesting. Journal of
700 Geophysical Research: Oceans, 118, 990–1002. doi:10.1002/jgrc.20077., 2013
- 701 Feng, Y., DiMarco, S. F., Balaguru, K., and Xue, H. Seasonal and interannual variability of areal extent
702 of the Gulf of Mexico hypoxia from a coupled physical-biogeochemical model: A new implication for
703 management practice. Journal of Geophysical Research: Biogeosciences, 124,1939–1960.
704 doi:10.1029/2018JG004745.,2019
- 705 Fong, D. A., and Geyer, W. R., Response of a river plume during an upwelling favorable wind event,
706 Journal of Geophysical Research-Oceans, 106(C1), 1067-1084, doi:10.1029/2000jc900134., 2001
- 707 Fong, D. A., and Geyer, W. R., The Alongshore Transport of Freshwater in a Surface-Trapped River
708 Plume, Journal of Physical Oceanography, 32(3), 957-972, doi:10.1175/1520-
709 0485(2002)032<0957:TATOFI>2.0.CO;2, 2002
- 710 Forget, G., Campin, J. M., Heimbach, P., Hill, C. N., Ponte, R. M. and Wunsch, C., ECCO version 4:
711 an integrated framework for non-linear inverse modeling and global ocean state estimation,
712 Geoscientific Model Development, 8(10), 3071-3104, doi:10.5194/gmd-8-3071-2015, 2015
- 713 Fournier, S., Reager, J. T., Lee, T., Vazquez-Cuervo, J., David, C.H., and Gierach, M. M., SMAP
714 observes flooding from land to sea: The Texas event of 2015, Geophysical Research Letter, 43,
715 L070821, doi:10.1002/2016GL070821, 2016



- 716 Fournier, S., Lee, T. and Gierach, M. M., Seasonal and interannual variations of sea surface salinity
717 associated with the Mississippi River plume observed by SMOS and Aquarius, Remote Sensing of
718 Environment, 180, 431 – 439. doi:10.1016/j.rse.2016.02.050, 2016
- 719 Fournier, S., Vialard, J., Lengaigne, M., Lee, T., Gierach, M. M., and Chaitanya, A. V. S. Modulation
720 of the Ganges-Brahmaputra river plume by the Indian Ocean dipole and eddies inferred from satellite
721 observations. Journal of Geophysical Research: Oceans, 122, 9591–9604. doi:10.1002/2017JC013333,
722 2017
- 723 Fournier, S., Vandemark, D., Gaultier, L., Lee, T., Jonsson, B., and Gierach, M. M. Interannual
724 variation in offshore advection of Amazon-Orinoco plume waters: Observations, forcing mechanisms,
725 and impacts. Journal of Geophysical Research: Oceans, 122, 8966–8982. doi:10.1002/2017JC013103,
726 2017
- 727 Fournier, S., Reager, J. T., Dzwonkowski, B., and Vazquez-Cuervo, J. Statistical mapping of
728 freshwater origin and fate signatures as land/ocean “regions of influence” in the Gulf of Mexico.
729 Journal of Geophysical Research: Oceans, 124, 4954–4973. doi:10.1029/2018JC014784, 2019
- 730 Friedlingstein, P., et al., Global Carbon Budget 2019, Earth System Science Data, 11, 1783-1838,
731 doi:10.5194/essd-11-1783-2019., 2019
- 732 García Berdeal, I., B. M. Hickey, and M. Kawase, Influence of wind stress and ambient flow on a high
733 discharge river plume, 107(C9), 13-11-13-24, doi:10.1029/2001jc000932.,2002
- 734 Garvine, R.W., Penetration of buoyant coastal discharge onto the continental shelf: a numerical model
735 experiment. Journal of Physical. Oceanography. 29, 1892–1909. doi:10.1175/1520-
736 0485(1999)029<1892:POBCDO>2.0.CO;2,1999
- 737 Garvine, R. W. The impact of model configuration in studies of buoyant coastal discharge. Journal of
738 Marine Research. 59, 193-225. doi:10.1357/002224001762882637, 2001
- 739 Gaspar, P., Grégoris, Y. & Lefevre, J.-M., A simple eddy kinetic energy model for simulations of the
740 oceanic vertical mixing: Tests at station Papa and long-term upper ocean study site, 95(C9), 16179-
741 16193, doi:10.1029/JC095iC09p16179, 1990
- 742 Gierach, M. M., Vazquez-Cuervo, J., Lee, T., and Tsontos, V. M., Aquarius and SMOS detect effects
743 of an extreme Mississippi River flooding event in the Gulf of Mexico, Geophysical Research Letter,
744 40, L50995. Doi:10.1002/grl.50995, 2013
- 745 Griffies, S. M., et al., Formulation of an ocean model for global climate simulations, Ocean Science,
746 1(1), 45-79, doi:10.5194/os-1-45-2005. 2005



- 747 Halliwell, G. R., Evaluation of vertical coordinate and vertical mixing algorithms in the HYbrid-
748 Coordinate Ocean Model (HYCOM), *Ocean Modelling*, 7(3), 285-322,
749 doi:10.1016/j.ocemod.2003.10.002.,2004
- 750 Herzfeld, M., Methods for freshwater riverine input into regional ocean models, *Ocean Modelling*, 90,
751 1-15, doi:10.1016/j.ocemod.2015.04.001.,2015
- 752 Huang, R. X., Real Freshwater Flux as a Natural Boundary Condition for the Salinity Balance and
753 Thermohaline Circulation Forced by Evaporation and Precipitation, *Journal of Physical Oceanography*,
754 23(11), 2428-2446, doi:10.1175/1520-0485(1993)023<2428:RFFAAN>2.0.CO;2, 1993
- 755 Kourafalou, V. H., Oey, L.-Y., Wang, J. D., and Lee, T. N., The fate of river discharge on the
756 continental shelf: 1. Modeling the river plume and the inner shelf coastal current, *Journal of*
757 *Geophysical Research*, 101(C2), 3415– 3434, doi:10.1029/95JC03024.,1996
- 758 IPCCs, Climate Change and Land: an IPCC special report on climate change, desertification, land
759 degradation, sustainable land management, food security, and greenhouse gas fluxes in terrestrial
760 ecosystems [P.R. Shukla, J. Skea, E. Calvo Buendia, V. Masson-Delmotte, H.-O. Pörtner, D. C.
761 Roberts, P. Zhai, R. Slade, S. Connors, R. van Diemen, M. Ferrat, E. Haughey, S. Luz, S. Neogi, M.
762 Pathak, J. Petzold, J. Portugal Pereira, P. Vyas, E. Huntley, K. Kissick, M. Belkacemi, J. Malley,
763 (eds.)]. In press. 2019
- 764 Jolliff, J. K., Kindle, J. C., Shulman, I., Penta, B., Friedrichs, M. A. M., Helber, R. and Arnone, R. A.,
765 Summary diagrams for coupled hydrodynamic-ecosystem model skill assessment, *Journal of Marine*
766 *Systems*, 76(1), 64-82, doi:10.1016/j.jmarsys.2008.05.014., 2009
- 767 Lacroix, F., Ilyina, T. and Hartmann, J., Oceanic CO₂ outgassing and biological production hotspots
768 induced by pre-industrial river loads of nutrients and carbon in a global modeling approach,
769 *Biogeosciences*, 17(1), 55-88, doi:10.5194/bg-17-55-2020.,2020
- 770 Landschützer, P., Gruber, N. and Bakker, D. C. E., Decadal variations and trends of the global ocean
771 carbon sink, *Global Biogeochemical Cycles*, 30(10), 1396-1417, doi:10.1002/2015GB005359.,2016
- 772 Landschützer, P., Laruelle, G. G., Roobaert, A., and Regnier, P.: A uniform pCO₂ climatology
773 combining open and coastal oceans, *Earth Syst. Sci. Data Discuss.*, doi: 10.5194/essd-2020-90, in
774 review, 2020
- 775 Lentz, S. J., The Amazon River plume during AMASSEDS: subtidal current variability and the
776 importance of wind forcing. *Journal of Geophysical Research – Oceans*, 100, 2377–2390,
777 doi:10.1029/94JC00343, 1995a
- 778 Lentz, S. J., Seasonal variations in the horizontal structure of the Amazon plume inferred from
779 historical hydrographic data. *Journal of Geophysical Research-Oceans*, 100, 2391–2400,
780 doi:10.1029/94JC01847, 1995b



- 781 Liao, X., Du, Y., Wang, T., Hu, S., Zhan, H., Liu, H. and Wu, G., High-Frequency Variations in Pearl
782 River Plume Observed by Soil Moisture Active Passive Sea Surface Salinity, Remote Sensing, 12, 563,
783 doi:10.3390/rs12030563, 2020
- 784 Liu, Y., MacCready, P. and Hickey, B. M., Columbia River plume patterns in summer 2004 as revealed
785 by a hindcast coastal ocean circulation model, Geophysical Research Letter, 36, L02601,
786 doi:10.1029/2008GL036447.,2009
- 787 Marshall, J., Adcroft, A., Hill, C., Perelman, L. and Heisey, C., A finite-volume, incompressible Navier
788 Stokes model for studies of the ocean on parallel computers, 102(C3), 5753-5766,
789 doi:10.1029/96jc02775.,1997
- 790 Mecklenburg, S., Drusch, M., Kerr, Y. H., Font, J., Martin-Neira, M., Delwart, S., . . . Crapolicchio, R.
791 ESA's soil moisture and ocean salinity mission: Mission performance and operations. IEEE
792 Transactions on Geoscience and Remote Sensing, 50, 1354–1366.
793 Doi:10.1109/TGRS.2012.2187666.,2012
- 794 Menemenlis, D., Hill, C. N., Adcroft, A. J., Campin, J.-M., Cheng, B., Ciotti, R. B., . . . Zhang, J.
795 NASA Supercomputer Improves Prospects for Ocean Climate Research. EOS Transactions AGU 86,
796 89–96. Doi:10.1029/2005EO090002,2005
- 797 Menemenlis, D., Campin, J.-M., Heimbach, P., Hill, C. N., Lee, T., Nguyen, A. T., . . . Zhang, H.
798 ECCO2: High Resolution Global Ocean and Sea Ice Data Synthesis. Mercator Ocean Quarterly
799 Newsletter, 31, 13–21.,2008
- 800 Molleri, G.S.F., Novo, E. M. L. M. & Kampel, M. Space-time variability of the Amazon River plume
801 based on satellite ocean color, Continental Shelf Research, 30, 342-352. [doi:10.1016/j.csr.2009.11.015](https://doi.org/10.1016/j.csr.2009.11.015),
802 2010
- 803 Neetu, S., Lengaigne, M., Vincent, E. M., Vialard, J., Madec, G., Samson, G., . . . Durand, F. Influence
804 of upper-ocean stratification on tropical cyclones-induced surface cooling in the Bay of Bengal. Journal
805 of Geophysical Research-Oceans, 117, C12020, doi:10.1029/2012JC008433,2012
- 806 Piecuch, C. G., & Wadehra, R. Dynamic sea level variability due to seasonal river discharge: A
807 preliminary global ocean model study. Geophysical Research Letters, 47, e2020GL086984.
808 Doi:10.1029/2020GL086984,2020
- 809 Rao, R. R., and Sivakumar, R. Seasonal variability of the salt budget of the mixed layer and near-
810 surface layer salinity structure of the tropical Indian Ocean from a new global ocean salinity
811 climatology. Journal of Geophysical Research-Oceans, 108, 3009. [doi:10.1029/2001JC000907](https://doi.org/10.1029/2001JC000907), 2003
- 812 Resplandy, L., Keeling, R.F., Rödenbeck, C., Stephens, B.B., Khatiwala, S., Rodgers, K.B., Long,
813 M.C., Bopp, L., Tans, P.P., Revision of global carbon fluxes based on a reassessment of oceanic and
814 riverine carbon transport. Nature Geoscience 1. doi: 10.1038/s41561-018-0151-3,2018



- 815 Roobaert, A., Laruelle, G. G. Landschützer, P., Gruber, N., Chou, L. and Regnier, P., The
816 Spatiotemporal Dynamics of the Sources and Sinks of CO₂ in the Global Coastal Ocean, *Global*
817 *Biogeochemical Cycles*, 33(12), 1693-1714, doi:10.1029/2019GB006239,2019
- 818 Roulet, G., and Madec, G., Salt conservation, free surface, and varying levels: A new formulation for
819 ocean general circulation models, 105(C10), 23927-23942, doi:0.1029/2000jc900089.,2000
- 820 Santini, M., and Caporaso, L. Evaluation of freshwater flow from rivers to the sea in CMIP5
821 simulations: Insights from the Congo River basin. *Journal of Geophysical Research: Atmospheres*, 123,
822 10,278–10,300. Doi:10.1029/2017JD027422,2018
- 823 Schiller, R. V., and Kourafalou, V. H., Modeling river plume dynamics with the HYbrid Coordinate
824 Ocean Model, *Ocean Modelling*, 33(1), 101-117, doi:10.1016/j.ocemod.2009.12.005.,2011
- 825 Seitzinger, S. P., Harrison, J. A., Dumont, E., Beusen, A. H. W., and Bouwman, A. F., Sources and
826 delivery of carbon, nitrogen, and phosphorus to the coastal zone: An overview of Global Nutrient
827 Export from Watersheds (NEWS) models and their application, *Global Biogeochemical Cycles*, 19,
828 GB4S01, doi:10.1029/2005GB002606.,2005
- 829 Seitzinger, S. P., Mayorga, E., Bouwman, A. F., Kroeze, C., Beusen, A. H. W., Billen, G., Drecht, G.
830 V., Dumont, E., Fekete, B. M., Garnier, J., and Harrison, J. A. Global river nutrient export: A scenario
831 analysis of past and future trends, *Global Biogeochemical Cycles*., 24, GB0A08,
832 doi:10.1029/2009GB003587.,2010
- 833 Sengupta, D., Goddalahundi, B. R., and Anitha, D. S. Cyclone-induced mixing does not cool SST in
834 the post-monsoon North Bay of Bengal. *Atmospheric Science Letters*, 9, 1–6.
835 Doi:10.1002/asl.162.,2008
- 836 Stammer, D., Ueyoshi, K., Köhl, A. Large, W.G., Josey, S. A., and Wunsch, C., Estimating air-sea
837 fluxes of heat, freshwater, and momentum through global ocean data assimilation, *Journal of*
838 *Geophysical Research*, 109(C5), doi:10.1029/2003jc002082.,2004
- 839 Su, Z., Wang, J., Klein, P., Thompson, A. F. and Menemenlis, D., Ocean sub mesoscales as a key
840 component of the global heat budget, *Nature Communications*, 9, 775, doi:10.1038/s41467-018-02983-
841 w.,2018
- 842 Suzuki, T., Yamazaki, D., Tsujino, H., Komuro, Y., Nakano, H., and Urakawa, S., A dataset of
843 continental river discharge based on JRA-55 for use in a global ocean circulation model, *Journal of*
844 *Oceanography*, 74(4), 421-429, doi:10.1007/s10872-017-0458-5.,2018
- 845 Timmermann, R., Danilov, S., Schröter, J., Böning, C., Sidorenko, D., and Rollenhagen, K., Ocean
846 circulation and sea ice distribution in a finite element global sea ice–ocean model, *Ocean Modelling*,
847 27(3), 114-129, doi:10.1016/j.ocemod.2008.10.009.2009



- 848 Tseng, Y.-h., Bryan, F. O. and Whitney, M. M., Impacts of the representation of riverine freshwater
849 input in the community earth system model, *Ocean Modelling*, 105, 71-86,
850 doi:10.1016/j.ocemod.2016.08.002.,2016
- 851 Tsujino, H., et al., JRA-55 based surface dataset for driving ocean–sea-ice models (JRA55-do), *Ocean*
852 *Modelling*, 130, 79-139, doi:10.1016/j.ocemod.2018.07.002.,2018
- 853 Volodin, E. M., Dianskii, N. A. and Gusev, A. V., Simulating present-day climate with the INMCM4.0
854 coupled model of the atmospheric and oceanic general circulations, *Izvestiya, Atmospheric and*
855 *Oceanic Physics*, 46(4), 414-431, doi:10.1134/S000143381004002X, 2010
- 856 Vialard, J., and Delecluse, P. An OGCM study for the TOGA decade. Part I: Role of salinity in the
857 physics of the western Pacific fresh pool. *Journal of Physical Oceanography*, 28, 1071–1088.
858 [doi:10.1175/1520-0485\(1998\)028<1071:AOSFTT>2.0.CO;2](https://doi.org/10.1175/1520-0485(1998)028<1071:AOSFTT>2.0.CO;2), 1998
- 859 Vinayachandran, P., Murty, V. S. N., and Ramesh Babu, V. Observations of barrier layer formation in
860 the Bay of Bengal during summer monsoon. *Journal of Geophysical Research-Oceans*, 107, 8018.
861 Doi:10.1029/2001JC000831,2002
- 862 Walker, N. D. Satellite assessment of Mississippi River plume variability: causes and predictability,
863 *Remote Sensing of Environment*, 58, 21-35. doi:10.1016/0034-4257(95)00259-6,1996
- 864 Ward, N.D., Megonigal, J.P., Bond-Lamberty, B. *et al.* Representing the function and sensitivity of
865 coastal interfaces in Earth system models. *Nature Communications* **11**, 2458 (2020).
866 <https://doi.org/10.1038/s41467-020-16236-2>.
- 867 Willmott, C. J., On the validation of models, *Phys. Geogr.*, 2, 184–194,
868 doi:10.1080/02723646.1981.10642213.,1981
- 869 Yueh, S. H., Tang, W., Fore, A. G., Neumann, G., Hayashi, A., Freedman, A., . . . Lagerloef, G. S. L-
870 band passive and active microwave geophysical model functions of ocean surface winds and
871 applications to Aquarius retrieval. *IEEE Transactions on Geoscience and Remote Sensing*, 51, 4619–
872 4632. doi:10.1109/TGRS.2013.2266915, 2013
- 873 Yueh, S. H., Tang, W., Fore, A., Hayashi, A., Song, Y. T., and Lagerloef, G. Aquarius geophysical
874 model function and combined active passive algorithm for ocean surface salinity and wind retrieval.
875 *Journal of Geophysical Research: Oceans*, 119, 5360–5379. doi:10.1002/2014JC009939, 2014
- 876 Zhang, H., Menemenlis, D. and Fenty, G. ECCO LLC270 Ocean-Ice State Estimate.
877 doi:1721.1/119821,2018
- 878 Aman, A. A., Cman, C., and Bman, B. B.: More test articles, *J. Adv. Res.*, 35, 13–28,
879 doi:10.2345/67890, 201